Photodissociation Dynamics of Gas-Phase $BrICl^-$ and IBr_2^- Anions

Andrei Sanov,[†] Todd Sanford, Laurie J. Butler,[‡] Jiri Vala,[§] Ronnie Kosloff,[§,||] and W. Carl Lineberger*

JILA, National Institute of Standards and Technology and University of Colorado, and Department of Chemistry and Biochemistry, University of Colorado, Boulder, Colorado 80309-0440

Received: June 23, 1999; In Final Form: August 23, 1999

This work is the first study of mixed trihalide anions in the gas phase. We report the photochemistry and photodissociation dynamics of $BrICl^-$ and IBr_2^- anions near 400 nm. For $BrICl^-$, two major photodissociation channels yielding IBr^- and ICl^- products are observed. The photodissociation of IBr_2^- yields primarily IBr^- anion products. No $BrCl^-$ and Br_2^- fragments are formed from $BrICl^-$ and IBr_2^-, respectively, and the parent anions are ascribed linear $[Br-I-Cl]^-$ and $[Br-I-Br]^-$ structures, in agreement with ab initio calculations. The IBr^- and ICl^- products are produced in highly vibrationally excited states. We observe fragment vibrational coherence in femtosecond pump−probe measurements by probing nascent IBr^- via its photodissociation to $I^- + Br$. The IBr^- vibrational periods observed in the photodissociation of $BrICl^-$ correspond to excitations of ∼80% of the IBr^- dissociation energy (D_o). In IBr_2^- dissociation, the average vibrational excitation of IBr^- is 84−91% of D_o. The high degrees of vibrational excitation raise questions about the effect of the proximity to the dissociation threshold on the dynamics of coherent wave packets. We analyze these dynamics analytically and by means of wave packet simulations and observe smearing of expected wave packet revivals.

I. Introduction

Detailed studies of gas-phase dynamics in small chemical systems serve as the foundation for understanding both gas-phase and condensed-phase chemistry. Comparison of gas-phase and cluster dynamics to behavior in solution allows for discerning the role of solvation in chemical reactions. One species playing a prominent role in modern chemistry as a model for testing physical theories is the triiodide anion, I_3^-. The recent studies of ultrafast dynamics of the photodissociation of I_3^- in solution[1−11] and in the gas phase[12−14] demonstrated vibrational coherence in the I_2^- fragment and yielded valuable information about dissipative phenomena involving highly excited molecules in solution. These experiments extended the earlier work on the photodissociation dynamics of HgI_2 in the gas phase[15−18] and in solution[19−22] and motivated broad theoretical research on vibrational coherence and wave packet dynamics with and without the effects of solvation.[23−29]

As attractive as they are from both experimental and fundamental viewpoints, the studies of the triiodide anion cannot be extended in some important ways. Because both I_3^- bonds are identical, it is impossible to exert control on the dissociation and achieve selective bond breaking. It is also difficult to determine experimentally the probability for electron localization on a given I atom in three-body $I_3^- \rightarrow 2I + I^-$ photodissociation. Only recently, through extensive modeling of time-dependent photoelectron spectra, have Neumark and co-workers shown that the I^- photofragment is most likely formed via concerted three-body dissociation along the I_3^- symmetric stretch coordinate.[13] In addition, the photofragment kinetic energy release measurements by the same group have indicated that in three-body dissociation the excess electron localizes on the middle I atom.[30]

The experimental task of identifying reaction pathways is simplified tremendously if the three atoms composing the trihalide anion are not identical. Compared to I_3^-, the photochemistry and dynamics of mixed trihalide anions is richer, because of an increased number of identifiable reaction pathways. In this publication, we report for the first time the efficient formation, photochemistry, and gas-phase photodissociation dynamics of two mixed trihalide anions: $BrICl^-$ and $BrIBr^-$. To this date, the only other studies of mixed trihalide anions are the work on the photodissociation of I_2Br^- and IBr_2^- in solution, currently in progress in the group of Ruhman.[7,31] In section III, we describe a straightforward method for preparing gas-phase $BrICl^-$ and $BrIBr^-$ which can be used to synthesize any trihalide anions of interest.

The first question about the mixed trihalide anions concerns their structure. Three different isomers of $BrICl^-$ are possible: $BrICl^-$, $IBrCl^-$, and $IClBr^-$. For IBr_2^-, two different species ($BrIBr^-$ and $IBrBr^-$) may exist on the ground-state potential energy surface. Structural isomers can complicate the analysis of photochemistry and dynamics beyond the possibility of detailed understanding. However, the results reported here dictate the following rule defining the minimum energy structures: the most stable isomer is the one with the heaviest atom in the middle. This rule is in accord with chemical intuition, and we expect it to be general for all mixed trihalides.

In interpreting the experimental results, we draw parallels with spectroscopy and dynamics of the triiodide anion. The UV absorption spectrum of I_3^- consists of two broad bands centered at 360 and 290 nm, and the solution-phase dissociation via either of these bands has been shown to yield I_2^- fragments.[4,9] In addition, the gas-phase experiment by Zanni et al. has indicated

[†] Present address: Department of Chemistry, The University of Arizona, Tucson, AZ 8521−0041.

[‡] JILA Visiting Fellow, Summer−Fall 1998. Permanent address: Department of Chemistry, The University of Chicago, Chicago, IL 60637.

[§] Permanent address: Department of Physical Chemistry and the Fritz Haber Center for Molecular Dynamics, The Hebrew University, Jerusalem, 91904 Israel.

[||] JILA Visiting Fellow Summer 1998−Summer 1999.

10.1021/jp9920803 CCC: $18.00
Published on Web 09/29/1999

the efficient production of I^-,[12,13] which was not observed in solution,[4,9] possibly because of the difficulty of detecting the closed-shell atomic fragment. The photodissociation of $BrICl^-$ reported here leads to two major fragment channels, $IBr^- + Cl$ and $ICl^- + Br$, which are equivalent to the I_2^- channel in I_3^-. The existence of two distinct pathways, probably evolving on the same electronic surface, is an attractive feature of asymmetric trihalides, raising a possibility for future studies of reaction control.

The femtosecond experiments on I_3^- in solution[1−11] and in the gas phase[12−14] revealed vibrational coherence in the I_2^- fragment with a varying degree of vibrational excitation. The solution-phase experiments demonstrated a distribution of photofragments with the average vibrational quantum number $\langle v \rangle = 12$,[2,4] which corresponds to an excitation of about ∼16% of the I_2^- dissociation energy (1.01 eV). In the gas phase, the average excitation was found to be much higher, ∼70% of the dissociation energy.[12,13] The difference is partly due to fast solvent-induced relaxation of I_2^- fragments in solution.

In accord with the I_3^- experiments, we observe vibrational coherence in the diatomic products of $BrICl^-$ and IBr_2^- photodissociation. The observed vibrational periods correspond to even greater product excitations than in the gas-phase photodissociation of I_3^-. The vibrational excitation can be controlled, among other factors, by varying the chemical identity of the parent trihalide anion. The comparison of ab initio results with experimental observations shows that the greater vibrational excitation of IBr^- fragments is at least partly due to the larger change in equilibrium I−Br bond length in the IBr^- product from that in the triatomic anion, as compared to the analogous change in I−I equilibrium bond lengths in $I_3^- \rightarrow I_2^- + I$ dissociation.

The high vibrational excitation of the photodissociation products raises the question of how the proximity to the dissociation threshold affects the dynamics of coherent vibrational wave packets. Far from the threshold, these dynamics in an isolated system usually can be described in terms of a classical vibrational period and a period of the so-called "revivals".[32,33] The initial wave packet created in an experiment is localized, and for a short time, it behaves classically.[34−36] The periodic oscillations in the experimental signal reflect the motion of the wave packet obeying the laws of Newtonian mechanics, for a short time. Following the short era of classical behavior, the wave packet spreads, and the vibrational motion can no longer be observed in a classical sense. However, if the vibrational level spacings decrease with the quantum number at a constant rate, the corresponding frequencies belong to a linear progression. Consequently, after a certain time, the oscillations at all different frequencies come back into phase with each other and another short era of classical behavior follows.[32,33]

This common picture of wave packet revivals depends on the assumption of first-order anharmonicity, which, strictly speaking, is only valid for the Morse oscillator. The behavior of real molecular systems far from the dissociation threshold can be approximated by this model, because deviations from the first-order anharmonicity are rather small. The situation changes radically near the threshold, where the level spacings become small and the anharmonicity changes rapidly with energy. In this case, the different frequencies involved in the near-threshold wave packet no longer belong to the same linear progression, even approximately. We analyze the problem of wave packet dynamics near the dissociation threshold in this paper.

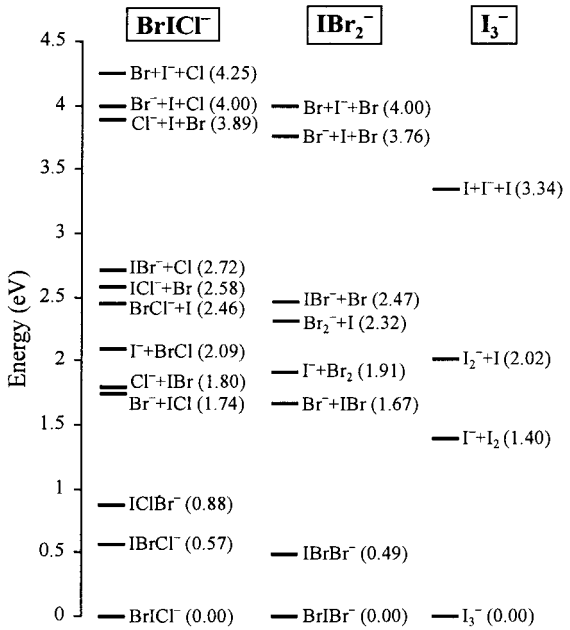

Figure 1. Energetics of the $BrICl^-$, IBr_2^-, and I_3^- anions, calculated using the *m*PW1PW density functional method, as described in the text. Numbers in parentheses are energies in electronvolts relative to the most stable isomer of the corresponding trihalide anion.

Since no previous data on the $BrICl^-$ and IBr_2^- anions are available, this Introduction is followed by a discussion of $BrICl^-$ and IBr_2^- energetics. We calculate the dissociation energies by an ab initio method and compare them to the energetics of I_3^-. Section III describes the experimental techniques and the apparatus. In particular, a method for efficient formation of $BrICl^-$ and IBr_2^- anions is described. Section IV presents the experimental results, including the mass-spectroscopic measurements of $BrICl^-$ and IBr_2^- photofragmentation and the femtosecond pump−probe measurements of the appearance and vibrational dynamics of diatomic photofragments. In Section V, we discuss the observed dissociation channels and possible mechanisms and analyze the vibrational dynamics of the IBr^- fragments.

II. Dissociation Energetics of $BrICl^-$ and IBr_2^- Anions

The zero-order energetics and structure of the $BrICl^-$ and IBr_2^- anions are investigated using density functional theory (DFT). The calculations are carried out with Gaussian 98[37] at the level of Barone and Adamo's Becke-style one-parameter exchange functional *m*PW1PW.[38] For open-shell and closed-shell systems, the spin-unrestricted and spin-restricted methods are used, respectively. For iodine, we use the relativistic effective core potential of Hay and Wadt,[39] combined with a double-ζ valence basis set (LanL2DZ). This basis is augmented with uncontracted diffuse s and p functions (exponents 0.0569 and 0.0330, respectively) and d and f polarization functions (exponents 0.292 and 0.441, respectively).[40] For bromine and chlorine, the 6-311+G(d) all-electron basis sets are used. For all species larger than an atom, the energies are calculated after full geometry optimizations.

The calculated energetics of the $BrICl^-$ and IBr_2^- anions are summarized in Figure 1. For comparison, also shown are the dissociation energies of I_3^- calculated by the same method. No attempt was made to account for the spin−orbit coupling. The zero-point vibrational energy corrections are not included. As expected, we find that the linear $[Br-I-Cl]^-$ isomer is the most stable form of $BrICl^-$. For all trihalides, the ground-state anion

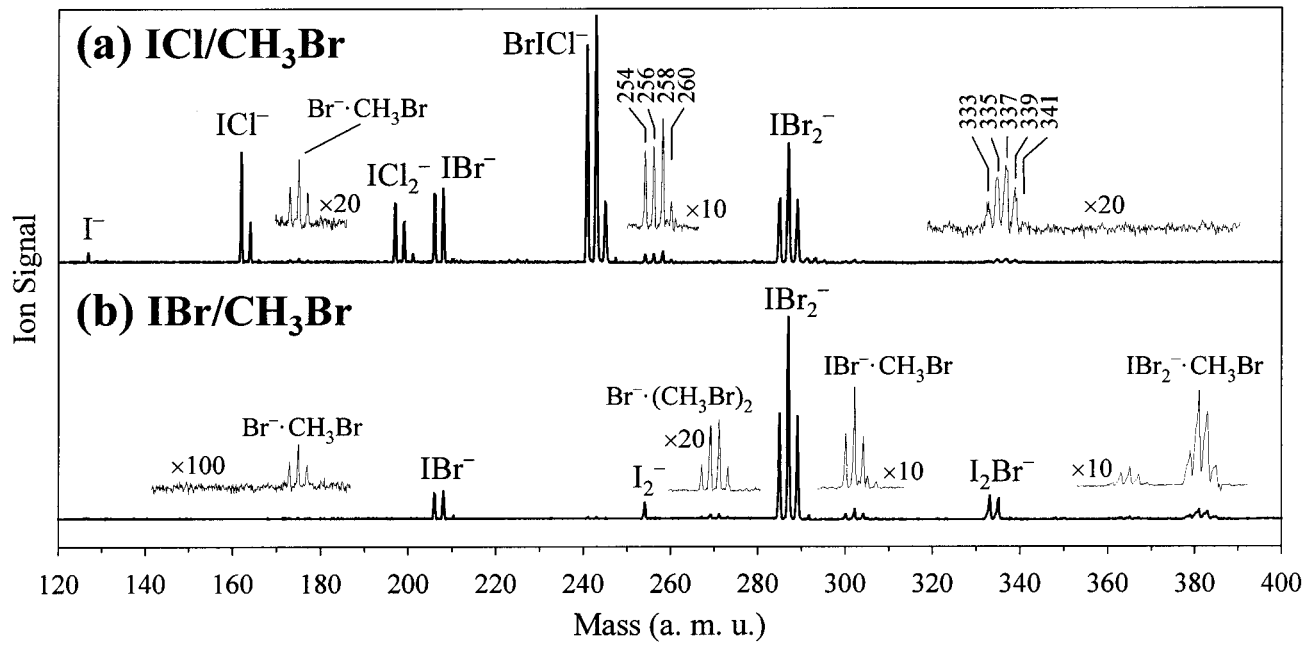

Figure 2. Mass spectra of precursor anions formed by coexpanding (a) ICl and CH_3Br seeded in Ar carrier gas, and (b) IBr and CH_3Br in Ar. Peaks in (a) labeled according to their masses are assigned as follows: $m = 254$ amu is I_2^-; 256, 258, and 260 are $ICl^-\cdot CH_3Br$; 333 and 335 are I_2Br^-, $m = 335$ overlaps the same mass of the quadruplet $m = 335$, 337, 339, and 341, assigned as $BrICl^-\cdot CH_3Br$.

TABLE 1: Vibrational Frequencies (in cm^{-1}) of Trihalides, Calculated Using the DFT (*m*PW1PW) Method, with Previous I_3^- Results Shown for Comparison

	*m*PW1PW[a]	QCISD(T)[b]	experiment[c]
$BrICl^-$	239.3		
	167.8		
	97.4		
$BrIBr^-$	170.2		
	156.1		
	76.4		
I_3^-	136.5	139.6	
	112.8	107.3	112 ± 1
	59.4	58.2	

[a] This work. [b] Calculations by Lynden-Bell et al.[28] [c] Experimental measurements by Zanni et al.[12,13] and Kaya et al.[64]

geometry is linear, with most of the charge localized on the two end atoms. The $BrICl^-$ configuration is stabilized relative to $IBrCl^-$ and $IClBr^-$ by the greater electronegativity of Cl and Br, compared to I, and by the screening effect of the large I atom, shielding the partially charged Cl and Br from each other. The next lowest configuration (the $IBrCl^-$ anion) is calculated to be 0.57 eV higher in energy. Similarly, $BrIBr^-$ is the most stable form of IBr_2^-, lying 0.49 eV lower than the $IBrBr^-$ anion. The vibrational frequencies of $BrICl^-$, $BrIBr^-$, and I_3^-, calculated using the *m*PW1PW method, are summarized in Table 1. Note the agreement between the calculated and measured[12,13] symmetric stretch frequencies of I_3^-.

By virtue of the state-of-the-art, our analysis does not include spin−orbit effects, which are expected to play major roles in both spectroscopy and dynamics. The spin−orbit splittings lead to the multiplicity of potentials in any one of the open-shell fragment channels in Figure 1. In addition, the DFT calculations overestimate the bond dissociation energies of open-shell species, in part, because of the omission of the spin−orbit effects. For example, in Figure 1, the dissociation energy of I_2^- is found to be 1.32 eV, compared to an experimental value of 1.01 eV.[41,42] The accuracy of the calculations is better for closed-shell species. For example, the bond strength of I_3^- for dissociation to the closed shell $I_2 + I^-$ products is calculated to be 1.40 eV, compared to 1.31 ± 0.06 eV measured in a collision-induced dissociation experiment by Do et al.[43]

III. Experiment

The tandem time-of-flight (TOF) ion beam apparatus has been described elsewhere.[44] The negative ions are formed and cooled in an electron impact ionized pulsed supersonic expansion[45] and mass analyzed in a Wiley−McLaren TOF mass spectrometer. To form $BrICl^-$, the gas sample for the supersonic expansion is prepared by passing a 5% mixture of CH_3Br in Ar over ICl kept at the room temperature. To preferentially form IBr_2^-, the ICl sample is substituted with IBr heated to about 40 °C to increase the vapor pressure. The resulting mixture is expanded into vacuum through a pulsed (80 Hz) supersonic nozzle (General Valve, Series 9) at a backing pressure of 3 atm. The expansion is crossed with a 1 keV electron beam close to the nozzle orifice. About 15 cm downstream from the nozzle, the anions are pulse extracted into the Wiley−McLaren TOF mass spectrometer.

Figure 2a shows a mass spectrum of precursor anions formed by co-expanding ICl and CH_3Br seeded in the Ar carrier gas. Figure 2b shows a corresponding mass spectrum for an IBr/CH_3Br expansion in Ar. The $BrICl^-$ and IBr_2^- anions correspond to the most intense peaks in the respective mass spectra. These anions are probably formed by attachment of slow secondary electrons to complex neutral clusters, as solvent evaporation and collisions remove the excess energy.[45] An alternative mechanism involving a solvent-assisted association of ICl or IBr with Br^- generated by dissociative electron attachment to CH_3Br (e.g., via a diabatic electron capture mechanism)[46−49] is also possible; however, a detailed discussion of the formation mechanism is beyond the scope of this paper. Several other ionic species are identified in Figure 2 and its caption, including other trihalide anions of interest, ICl_2^- and I_2Br^-. We expect that the formation efficiency of the later anion will increase in an I_2/CH_3Br expansion.

The triplet structures of the $BrICl^-$ and IBr_2^- peaks in Figure 2 (masses 241, 243, 245 and 285, 287,289, respectively) reflect

the existence of the isotopes of $^{79,81}Br$ and $^{35,37}Cl$ (while ^{127}I is the only major natural isotope of iodine). The natural abundance ratios of $^{79}Br/^{81}Br \approx 1:1$ and $^{35}Cl/^{37}Cl \approx 3:1$ dictate the following intensity patterns for the $BrICl^-$ and IBr_2^- peaks: $^{79}BrI^{35}Cl^-/(^{79}BrI^{37}Cl^- + {}^{81}BrI^{37}Cl^-)/{}^{81}BrI^{37}Cl^- \approx 3:4:1$ and $^{79}BrI^{79}Br^-/{}^{79}BrI^{81}Br^-/{}^{81}BrI^{81}Br^- \approx 1:2:1$. The isotope patterns for these and other ions are helpful in assigning the peaks in the mass spectra. For example, the group of four peaks (m = 379, 381, 383, and 385) in Figure 2b labeled as $IBr_2^-\cdot CH_3Br$ reveals a deviation from the statistically expected isotope ratio of 1:3:3:1. The excessive intensity of the $m = 381$ peak is most likely due to a contribution from I_3^-.

At the spatial focus of the Wiley−McLaren mass spectrometer, the ion beam is crossed with a beam of pulsed laser radiation synchronized to interact only with ions of the desired mass. Other ions are deflected out of the ion beam by a pulsed electrostatic mass gate, positioned before the crossing with the laser beam.

The ionic photofragments are analyzed using a second, reflectron mass spectrometer,[50,51] which is tilted at a small angle with respect to the primary ion beam axis. The fragments are detected at the spatial focus of the reflectron with a microchannel plate (MCP) detector. The ion signal is amplified and sent to either a transient digitizer for averaging or a gated threshold discriminator for single ion counting. The precursor ion signal is simultaneously monitored with another MCP detector positioned behind the reflectron.

The laser radiation is generated by one of two femtosecond systems. Each system is based on the same Coherent Mira Ti:sapphire oscillator pumped by a Coherent Nova 90 Ar ion laser. The oscillator output is selectively amplified in an Excel Quantronix femtosecond amplifier. One amplifier system has been described elsewhere.[52] A combination of a Series 4800 stretcher/compressor and a Ti:sapphire-based regenerative amplifier pumped by a 10 mJ/pulse Nd:YLF laser delivers 1 mJ, 120 fs pulses with a 400 Hz repetition rate in the vicinity of 800 nm. The other, new amplifier has similar output characteristics, with the notable exception of a 3 mJ pulse energy. This system, also from Quantronix, includes a pulse stretcher, a Ti:sapphire-based regenerative amplifier, a second multipass amplifier, and a pulse compressor. The dual amplification system is pumped by a 20 mJ/pulse Nd:YLF laser. In the reported experiments, the output pulse duration from this system varied between 120 and 160 fs.

Two-thirds of the laser output is used unmodified as a visible/near-IR probe, while the rest is frequency doubled in a 0.1 mm thick BBO crystal to generate an up to 300 μJ/pulse near-UV pump. The pump beam passes through a computer controlled delay stage, and the two beams, having parallel polarizations, are recombined using a dichroic beam splitter. The beams are collimated to 2−3 mm diameter and copropagate through the ion interaction region. Background subtraction is performed using computer-controlled shutters in the pump and probe beam paths. To better average out fluctuations, the data acquisition algorithm includes a rapid repetition of identical cycles of several preset pump−probe delays interlaced with background acquisitions. The zero of the delay is found by maximizing the pump−probe sum frequency generation in a KDP crystal before the vacuum chamber entrance window and after the identical exit window and then taking the average of the two measurements. The total experimental time resolution (the cross-correlation width of the pump and probe pulses after passing through optics and the chamber window) is estimated at ~300 fs. The one-photon fragmentation is performed using the femtosecond laser by blocking the near-IR probe beam, except for $BrICl^-$ measurements at $\lambda = 350-380$ nm, for which we used the frequency doubled output of a Quanta-Ray Nd:YAG laser pumped PDL-1 dye laser (~5 ns, 0.7 mJ pulses).

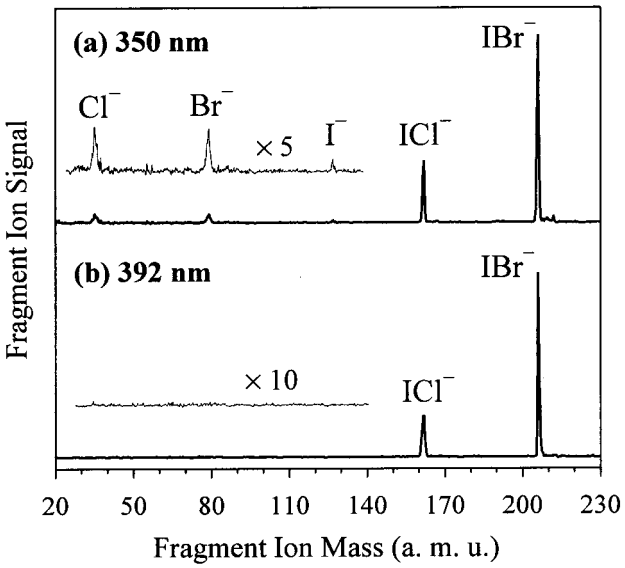

Figure 3. Photofragment ion mass spectra obtained in the photodissociation of $BrICl^-$ (the $^{79}BrI^{35}Cl^-$ isotope) at (a) 350 nm and (b) 392 nm.

IV. Experimental Results

A. Photodissociation of $BrICl^-$. The photodissociation experiments on $BrICl^-$ are carried out by mass-selecting the $^{79}BrI^{35}Cl^-$ ($m = 241$) isotope corresponding to the first peak of the $BrICl^-$ triplet in Figure 2a. The photofragment ion mass spectra of $BrICl^-$ obtained at 350 and 392 nm are shown in parts a and b of Figure 3, respectively. At all wavelengths studied (350−410 nm), the IBr^- and ICl^- fragments account for >95% of the photodissociation. Notably, no $BrCl^-$ fragments ($m = 114$) are ever observed, indicating that only the $BrICl^-$ species is formed in the ion source, with no noticeable contributions of $IBrCl^-$ and $IClBr^-$. This conclusion is in accord with the theoretical findings in section II, indicating that $BrICl^-$ is the most stable form of the anion and the energy gap separating it from the next energetically lowest isomer, $IBrCl^-$, is large.

At all wavelengths studied, IBr^- is the dominant photofragment with the fractional yield slightly decreasing with the photon energy from 0.8 at $\lambda = 405$ nm to <0.7 at $\lambda = 350$ nm. The remaining dissociation trajectories mostly lead to the ICl^- + Br channel, whose fractional yield increases with energy from 0.2 at $\lambda = 405$ nm to 0.3 at $\lambda = 350$ nm. As seen in Figure 3, the atomic anion fragments Cl^-, Br^-, and I^-, accounting for ~5% of the total photodissociation yield at $\lambda = 350$ nm, disappear at longer wavelengths.

The time-resolved dynamics of $BrICl^-$ photodissociation are studied by probing the IBr^- and ICl^- photofragments with the delayed fundamental output of the laser (780−820 nm). In preliminary experiments with the nanosecond laser, the near-IR absorption spectrum of IBr^- was found to be similar to that of I_2^-, with an absorption band around 700−750 nm. The dominant ionic fragment of IBr^- dissociation via this band is I^-; for example, at 720 nm I^- accounts for >98% of the total dissociation yield. Unlike IBr^-, the photodissociation of ICl^- has been studied previously.[44,53] Its red absorption band peaks near 700 nm and tails off to <20% of the maximum intensity

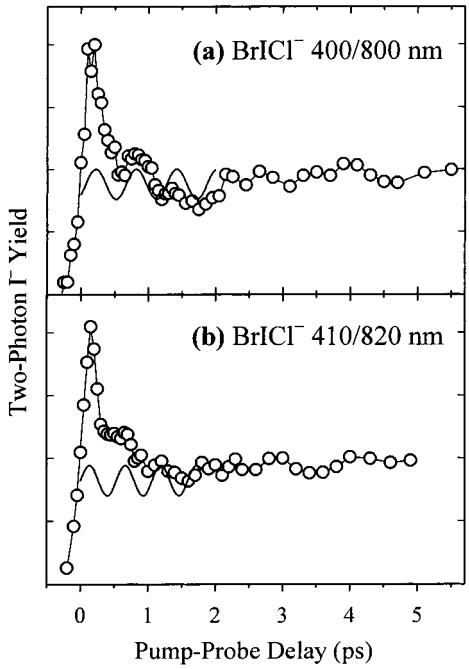

Figure 4. Delay-dependent pump−probe signals in the photodissociation of $BrICl^-$ to IBr^- + Cl and ICl^- + Br, probing the dynamics of the IBr^- and ICl^- products by further dissociating them to I^- + Br(Cl) and monitoring the delay-dependent yield of pump−probe I^- fragments: (a) 400 nm pump/800 nm probe; (b) 410 nm pump/820 nm probe. The superimposed sine waves highlight the oscillations in the experimental signal. The corresponding approximate periods are 600 fs in (a) and 530 fs in (b).

at $\lambda \geq 750$ nm. Similar to IBr^-, the I^- fragment dominates the photodissociation of ICl^- via this band, accounting for 94% of ionic photofragments at 740 nm.[44,53]

In the pump−probe experiment, the ~400 nm pump dissociates $BrICl^-$ to form IBr^- and ICl^- fragments (see Figure 3b), which are then dissociated by the ~800 nm probe pulse to yield predominantly I^- fragments. We monitor the two-photon (pump−probe) yield of I^- as a function of pump−probe delay. Figure 4 shows the resulting time-dependent signals measured with 400 nm pump/800 nm probe and 410 nm pump/820 nm probe. Both IBr^- and ICl^- produced in the photodissociation of $BrICl^-$ are formed in highly excited vibrational states, which may efficiently absorb light to the red of the absorption maxima of relaxed IBr^- and ICl^-. In the time-dependent dynamics shown in Figure 4, we do not resolve the contributions of the IBr^- and ICl^- channels to the pump−probe I^- signal. However, we attribute most of the observed signal to IBr^-. While this assumption suffers from the lack of knowledge of the relative absorption cross sections of the highly excited vibrational states of $IBr^-$and ICl^-, it is reasonable based on the 3−4 times greater observed yield of IBr^- relative to that of ICl^-.

The sharp initial peaks in parts a and b of Figure 4, with the rise times determined by the time resolution, may be partially attributed to the probe photon absorption by an excited state of $BrICl^-$. However, if the dissociation is direct, this excited-state correlates with the IBr^- + Cl and/or ICl^- + Br channel(s). Therefore, the initial peak may be viewed as arising from the probe-photon absorption by IBr^- (ICl^-) perturbed by the proximity of the Cl (Br) neutral fragment. Alternatively, a part of the initial absorption may be attributed to the excited $BrICl^-$, while the rest is due to the IBr^- (ICl^-) fragment.

Following the initial peak, several periodic oscillations are discernible in the signal in Figure 4. To highlight these oscillations, the experimental curves are superimposed with sine waves with periods of 600 fs in Figure 4a and 530 fs in Figure 4b. The oscillations are attributed to the motion of an IBr^- wave packet created in the impulsive dissociation of $BrICl^-$.

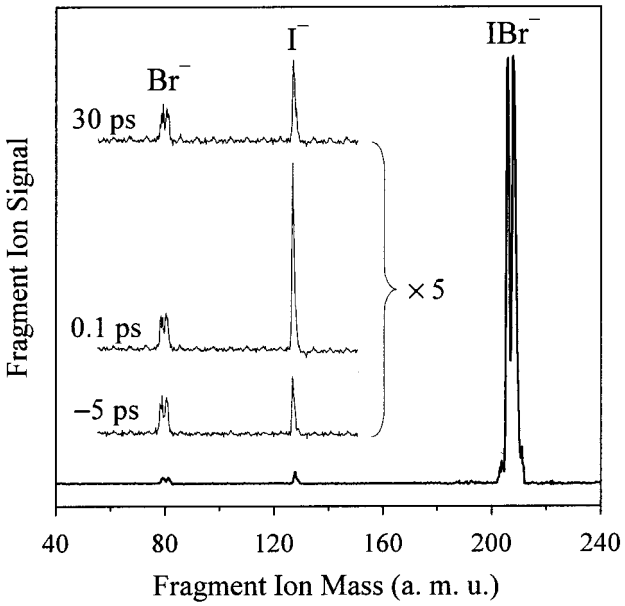

Figure 5. Bold line: photofragment ion mass spectrum in the photodissociation of IBr_2^- (the $^{79}BrI^{81}Br^-$ isotope) at 402 nm. Thin lines: portions of the photofragment mass spectra obtained with the pump (402 nm) and probe (804 nm) beams combined at indicated delays.

B. Photodissociation of IBr_2^-. The one-photon photofragmentation experiments on IBr_2^- and time-resolved measurements at short delays (<10 ps) were carried out on the $^{79}BrI^{81}Br^-$ ($m = 287$) isotope, which corresponds to the most intense peak of the IBr_2^- triplet in Figure 2b. A photofragment ion mass spectrum of IBr_2^- obtained at 402 nm is shown in Figure 5 (bold line). As in the case of $BrICl^-$, diatomic anion fragments (IBr^-) account for >95% of the photodissociation, and the Br_2^- fragment is not observed. In agreement with the ab intio findings in section II, this result indicates that only the most stable isomer, the $BrIBr^-$ species, is produced in the ion source, with no noticeable contributions of $IBrBr^-$.

A small fraction of the IBr_2^- dissociation yield (<5%) leads to atomic anion fragments Br^- and I^-. Unlike $BrICl^-$, these fragments do not disappear at lower photon energies up to 410 nm. The photofragment mass spectrum shown by the bold line in Figure 5 is representative of photodissociation in the entire 390−410 nm range. We also carried out a measurement using a combination of 391 and 261 nm pulses (second and third harmonics) and observed a manyfold (>10) increase in the yield of I^- compared to that shown in Figure 5. Because the 261 nm light leads to the photodetachment of the 391 nm fragment, IBr^-, rather than its dissociation, the observed increase in the I^- yield is attributed to the photodissociation of IBr_2^- at 261 nm.

The time-resolved dynamics of IBr_2^- photodissociation at 390−410 nm are studied using the same approach as described for $BrICl^-$. The appearance and vibrational dynamics of the IBr^- photofragment are probed at varied delay with the fundamental laser output (~800 nm), which further dissociates the IBr^- fragment to yield primarily I^-. Unlike $BrICl^-$, where the observed two-photon signal can originate from both IBr^- and ICl^- one-photon fragments, there is no ambiguity in the case of IBr_2^-. However, because the asymmetric $^{79}BrI^{81}Br^-$ isotope is mass selected in the experiment, the observed two-photon signal derives equally from the $I^{79}Br^-$ and $I^{81}Br^-$ one-

photon fragments (see the IBr^- doublet in Figure 5). The vibrational frequencies of the two IBr^- isotopes differ by only 0.77%, and thus the short-term (<10 ps) vibrational dynamics are unaffected by the superposition of the two frequencies. However, the mismatch becomes important on time scales of tens of picoseconds.[54]

The two-photon I^- signal is superimposed upon the one-photon I^- from IBr_2^- dissociation by the pump beam. The thin lines in Figure 5 show portions of the photofragment mass spectra obtained in the pump (402 nm) and probe (804 nm) measurements at different delays. The bottom spectrum, recorded with the probe pulse arriving 5 ps *before* the pump, is similar to the pump-only mass spectrum shown by the bold line, because the probe radiation is not absorbed by IBr_2^-. The middle trace, obtained at a 0.1 ps delay, shows a marked increase in the I^- intensity resulting from the two-photon formation of this fragment. The Br^- intensity remains unaffected because mostly I^- is produced in IBr^- dissociation in the near-IR. At longer delays, the intensity of the I^- peak reduces again but stays above the one-photon background level.

The time delay dependence of the two-photon I^- signal (with the one-photon background subtracted) is shown in Figure 6 for three different combinations of the pump and probe wavelengths. The overall patterns are similar to those observed in $BrICl^-$, however, the intensity of the initial peak compared to the long-delay signal is markedly greater in IBr_2^-. This intensity exhibits a downtrend with increasing pump and probe wavelengths. The reduction may be due to a decrease in the excited-state absorption in IBr_2^-, or alternatively, due to an increase in the probe absorption by vibrationally excited IBr^-.

Similar to $BrICl^-$, periodic oscillations in the pump−probe I^- signal are observed and attributed to IBr^- vibrational motion. In Figure 6, these oscillations are highlighted with sine waves superimposed with the experimental curves. The oscillation periods that best describe the experimental curves exhibit a decreasing trend with increasing pump and probe wavelengths, about 800 fs for 391 nm pump/782 nm probe (Figure 6a), 650 fs for 402/804 nm (Figure 6b), and 620 fs for 407/814 nm (Figure 6c). This trend likely reflects the excitation and probing of progressively lower vibrational levels in IBr^-.

The IBr_2^- anion presents a good system for studying the long-term wave packet dynamics. Unlike $BrICl^-$, where the I^- pump−probe fragments may be formed via both the IBr^- and ICl^- channels, in the case of IBr_2^- there is only one intermediate fragment, IBr^-. We unsuccessfully searched for the revival of the vibrational wave packet by mass-selecting the $I^{79}Br_2^-$ parent anion and scanning the pump−probe delay in the vicinities of 18 and 29 ps, as predicted in section V.C. Our inability to observe wave packet revivals in IBr^- may be due to several factors. Among them are insufficient time resolution, smearing out the weak revival signal (see the weak oscillations observed at short delays); and possibly the smearing of the revivals themselves due to several sources discussed in section V.C.

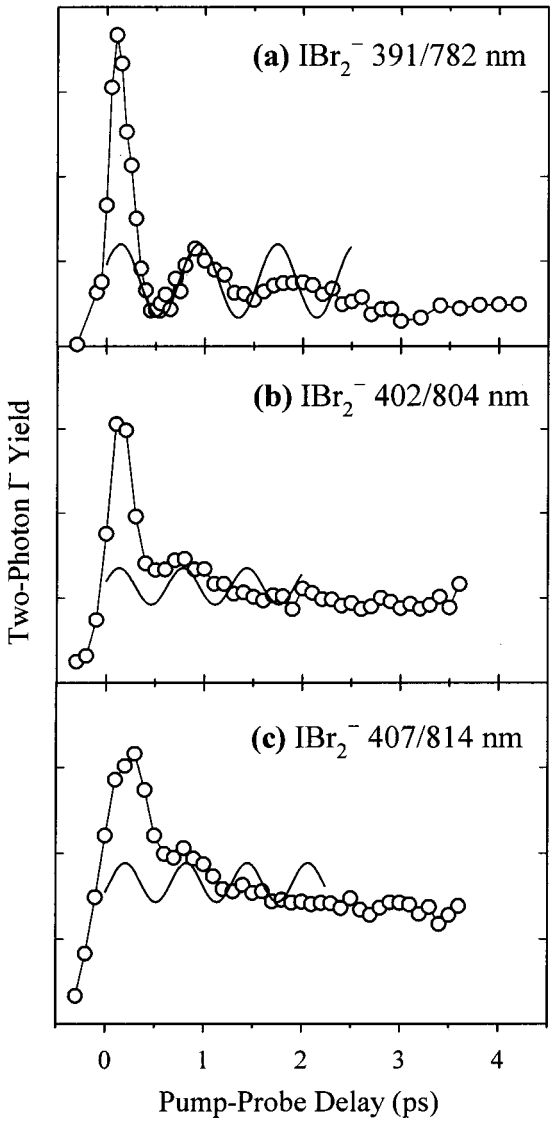

Figure 6. Delay-dependent pump−probe signals in the photodissociation of IBr_2^-, obtained by probing the dynamics of IBr^- products by further dissociating them to $I^- + Br$ and monitoring the delay-dependent yield of I^-: (a) 391 nm pump/782 nm probe; (b) 402 nm pump/804 nm probe; (c) 407 nm pump/814 nm probe. The superimposed sine waves highlight the oscillations in the experimental signals. The corresponding approximate periods are 800 fs in (a), 650 fs in (b), and 620 fs in (c).

V. Discussion

A. Dissociation Channels and Mechanisms. The photofragmentation pattern of $BrICl^-$, yielding primarily IBr^- and ICl^-, but no $BrCl^-$, indicates that only the I-centered isomer of $BrICl^-$ is produced in the ion source. Similarly, the fragmentation of IBr_2^- to $Br + IBr^-$, but never to $Br_2^- + I$, indicates that the symmetric $BrIBr^-$ isomer is the only IBr_2^- species in the parent ion beam. These conclusions are in accord with the ab initio results in section II.

The propensity toward the IBr^- fragment in the case of $BrICl^-$ indicates that the excited-state potential energy surface has a larger gradient in the direction of the I−Cl stretch compared to the I−Br stretch. The existence of two distinct major channels accessed by the same transition opens a possibility for future experiments to control the branching ratio by laser-shaping the excited-state wave function to favor one or the other channel.

An important distinction between the $BrICl^-$ and IBr_2^- results and the previous studies of gas-phase I_3^- is that in the latter case similar yields of the diatomic (I_2^-) and atomic (I^-) fragment anions were observed at 390 nm.[12,13] In contrast, for $BrICl^-$ and IBr_2^-, the atomic anion fragments account for <5% of the total near-UV dissociation yield.

In the case of gas-phase I_3^-, three-body dissociation has been implicated by Neumark and co-workers in the formation of the I^- fragment.[12,13] According to Figure 1, the $I + I^- + I$ dissociation channel lies slightly above the 3.2 eV energy of 390 nm photons used in the experiment. However, as pointed out in section II, the DFT calculations overestimate the bond

dissociation energies. We concur that the $I + I^- + I$ channel is energetically accessible in the Neumark experiment and likely accounts for the large yield of I^-. However, the respective pathways in $BrICl^-$ and IBr_2^- are higher in energy than in I_3^- (see Figure 1) and it is unclear whether they are accessible in our experiments. Because of this uncertainty, we cannot confidently rule in or out the three particle pathways as the source of the atomic anion fragments in the photodissociation of $BrICl^-$ and IBr_2^- at 3.0−3.5 eV. The atomic anion fragments can also be formed by a sequential mechanism involving the formation of IBr^- or ICl^- fragments in excited states, which further break up to form the atomic fragments. This mechanism requires as much energy as the direct three-body dissociation.

The small yield of atomic anion fragments is either an indication of a dynamically constrained dissociation mechanism or a result of the energetic proximity to the channel threshold (small RRKM rate). A stringent dynamical constraint hardly applies to the three-body dissociation, since the production of I^- in a three-body photodissociation of I_3^- is very efficient,[12,13] but the threshold proximity and competition with other dissociation channels can explain the small three-body dissociation yield. However, an RRKM-type argument runs into difficulty if one considers the similar yields of I^- and Br^- from IBr_2^-, despite the 0.24 eV energy gap between the $Br + I^- + Br$ and $Br^- + I + Br$ channel thresholds (see Figure 1). Thus, the observed small yields of atomic anion fragments of $BrICl^-$ and IBr_2^- favor a different, indirect mechanism of their formation, other than the three-body dissociation.

An additional dynamical argument against the three-body dissociation near 400 nm is the observation of a marked increase in the I^- yield from IBr_2^- at 261 nm (4.75 eV). This result indicates that when the three-body pathway does open, it leads to preferential charge localization on the middle atom of the parent anion, that is I^-. This is not what is observed at longer wavelengths; the yields of I^- and Br^- from IBr_2^- at ∼400 nm are comparable (Figure 5), while for $BrICl^-$, the 350 nm yield of I^- is, to the contrary, smaller than that of Cl^- and Br^- [Figure 3a]. However, it is possible that different electronic states of the parent are accessed at ∼400 and 261 nm, which may lead to different types of three-body dissociation.

Thus, further studies are needed to determine conclusively whether the atomic anion fragments observed in the near-UV dissociation of $BrICl^-$ and IBr_2^- are formed via three-body breakup channels. On the basis of the available evidence, the lower two-body channels yielding an atomic anion and a neutral diatom (see Figure 1) are as likely to be responsible for the observed Br^- and Cl^- fragments. In this case, the small yield of these fragments can be explained by an indirect mechanism involving internal conversion from the bright state, which itself does not correlate with these dissociation channels. Additionally, the observed highly excited IBr^- fragments open a possibility that some of the Br^- fragments are formed by subsequent dissociation of some of the initial IBr^- excited above the $Br^- + I$ dissociation threshold.

The two-body $I^- + BrCl$ or $I^- + Br_2$ pathways are less likely to account for the observed I^- fragments. Given the $[Br-I-Cl]^-$ and $[Br-I-Br]^-$ structures of the parent anions, these pathways require significant nuclear rearrangement and the bond formation between initially separated atoms. Although not very likely, such mechanism is not impossible considering the bent structures of some of the excited states of trihalides and the observed very small yields of I^-.

B. Vibrational Dynamics of IBr^- Fragments. Upon photodissociation of a trihalide anion to a diatomic anion and an atom, the antibonding excess electron, which is delocalized between two bonds in the ground state of the parent, localizes on a single bond of the diatomic fragment. In the valence picture, both bonds in IBr_2^- and I_3^- are of ∼3/4 order, while in the IBr^- and I_2^- fragments, the bond order is reduced to $^1/_2$. Thus, the I−Br and I−I bonds in the diatomic anion fragments are initially compressed relative to the relaxed diatomic and the fragments are formed in vibrationally excited states at a short bond length. The same is true for $BrICl^-$ dissociating to $IBr^- + Cl$ and $ICl^- + Br$.

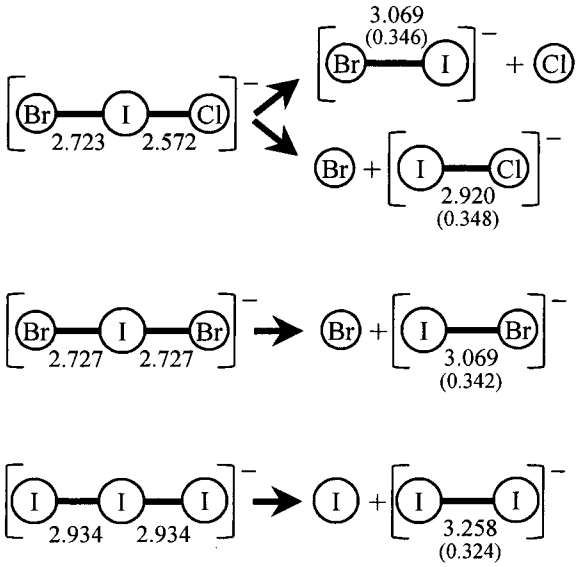

Figure 7. Equilibrium geometries of the $BrICl^-$, IBr_2^-, and I_3^- anions and their fragments, calculated using the *m*PW1PW method, as described in section II. Bond lengths are in angstroms. Numbers in parentheses indicate the bond elongation upon dissociation of the respective trihalide anion.

Figure 7 shows the equilibrium bond lengths of $BrICl^-$, IBr_2^-, I_3^-, along with the IBr^-, ICl^-, and I_2^- fragments, calculated using the DFT method described in section II. The numbers in parentheses indicate the bond elongation upon dissociation of the respective parent trihalide anion. On the basis of these calculations, we expect higher vibrational excitation in IBr^- and ICl^- formed in the photodissociation of $BrICl^-$ and IBr_2^-, compared to the I_2^- fragment of I_3^-.

The periodic oscillations observed in the pump−probe measurements on $BrICl^-$ (Figure 4) and IBr_2^- (Figure 6) are attributed to the wave packet motion on the IBr^- potential. Because the pump pulse is shorter than the IBr^- fragment vibrational period, the fragment formed is a coherent superposition of vibrational levels. The IBr^- absorbs the probe light when the initially compact wave packet passes through an absorption window, which is likely localized on the outer wall of the potential. Following several round-trips, the wave packet delocalizes, because of the anharmonicity of the potential, and the signal oscillations cease. (In the case of $BrICl^-$, there may also be a contribution of ICl^- fragment to the two-photon I^- signal. Here, we neglect this possibility taking into account the ∼4:1 branching ratio of one-photon IBr^- and ICl^- fragments.) The observed vibrational periods range from about 530 to 600 fs for $BrICl^-$ photodissociation and from 620 to 800 fs for IBr_2^-, corresponding to frequencies of 63 to 56 cm^{-1} and 54 to 42 cm^{-1}, respectively.

The ground-state vibrational frequency of IBr^- has been recently measured to be $\omega_o = 136$ cm^{-1}.[31] Within the Morse oscillator model, the classical vibrational frequency scales as

$$\omega(E) = \omega_o(E/D_o)^{1/2} \quad (1)$$

where D_o is the dissociation energy and E is the energy below the $I + Br^-$ threshold (i.e., the vibrational energy $E_v = D_o - E$). Using eq 1, the frequencies of 63 to 56 cm^{-1} observed in $BrICl^-$ dissociation correspond to average vibrational excitations ranging from 0.79 to 0.83 of the IBr^- dissociation energy ($D_o \approx 1$ eV). For IBr_2^- dissociation, the observed range of vibrational frequencies (54−42 cm^{-1}) corresponds to excitations of 0.84 to 0.91 of D_o.

In comparison, Zanni et al. observed coherent I_2^- vibration with a period of 550 fs (60 cm^{-1}) in the photodissociation of I_3^- at 390 nm.[12,13] Given the 110 cm^{-1} ground-state I_2^- vibrational frequency,[42] the observed oscillations correspond to an average vibrational excitation of 0.7 of the I_2^- dissociation energy.

To simulate the dynamics of highly excited vibrational states, a high quality IBr^- potential is needed. Figure 8a (symbols) shows the potential calculated using second-order Møller−Plesset perturbation theory (MP2).[55−57] The symbols in Figure 8b show the potential obtained by quadratic configuration-interaction calculation, including single and double excitations (QCISD).[58] Both calculations rely on the spin-unrestricted Hartree−Fock method and employ the basis sets described in section II.[37] We caution that both calculations do not account for the spin−orbit coupling. The parameters of both potentials are summarized in Table 2. The MP2 calculation predicts the IBr^- bond dissociation energy $D_o = 1.04$ eV and the ground-state vibrational frequency $\omega_o = 136.8$ cm^{-1}, the latter parameter being in agreement with the recent experiment of Gershgoren and Ruhman (136 cm^{-1}).[31] The QCISD calculation predicts $D_o = 0.95$ eV and $\omega_o = 127.4$ cm^{-1}. The solid lines in parts a and b of Figure 8 represent the Morse-potential fits with the parameters given in Table 2. Both the MP2 and QCISD potentials exhibit marked deviations from the respective Morse fits at the long range. This is not surprising, because the long-range IBr^- potential is best characterized by the ion−neutral interaction scaling as R^{-4}, whereas the Morse potential scales exponentially with distance. Both the MP2 and the QCISD potentials approximately follow the R^{-4} scaling in the intermediate distance range from ∼5 to 9 Å but deviate from it at larger distances. The deviations are attributed to the difficulties associated with calculating the electronic wave functions at such large separations.

We observe that the average fragment vibrational excitation in $BrICl^-$ and IBr_2^- photodissociation is greater than that in the case of I_3^-. The degree of vibrational excitation depends on the geometry change upon dissociation, the energetics and structure of the excited electronic states, and the excitation energy. According to the optimized geometries in Figure 7, the elongation of the I−Br bond in $BrICl^-$ and IBr_2^- dissociation is ∼0.02 Å greater than the corresponding elongation of the I−I bond in I_3^- dissociation. Seemingly insignificant, the extra 0.02 Å of impulsive bond stretching corresponds to an additional vibrational excitation of $\sim 0.1D_o$ if one considers the IBr^- inner potential wall gradient at $E_v \approx 0.8$ eV (Figure 8) and assumes a similar gradient for the I_2^- potential. Therefore, among other factors, the bond elongation may account for the higher fragment excitation in our experiments.

C. Wave Packet Dynamics near Dissociation Threshold. The revivals of the IBr^- wave packet, which we were unable to observe, may be smeared because of the decay of the revival structure itself. While we cannot rule out experimental factors (i.e., insufficient time resolution) as being responsible for the lack of revivals in the data, other possible sources include rotational dephasing and the multiplicity of the spin−orbit surfaces asymptotically accessed in the dissociation. However, we are cautious about considering these factors, because Neumark and co-workers did observe wave packet revivals in a similar system (I_3^-) and under similar experimental conditions.[12,13]

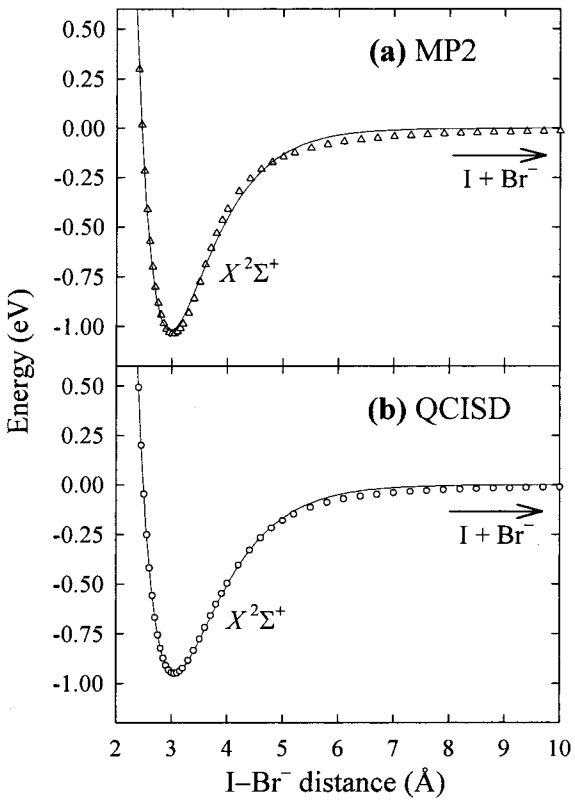

Figure 8. Symbols: the ground electronic state IBr^- potential calculated using the (a) MP2 and (b) QCISD methods, as described in the text. Lines: least-squares fits to the calculated potentials with a Morse function. Parameters of the two potentials and their respective Morse fits are summarized in Table 2.

TABLE 2: Parameters of the MP2 and QCISD Potentials of IBr^- and Their Fits with a Morse Function, as Shown in Figure 8

	MP2	QCISD
Potential Parameters		
D_o, dissociation energy, eV	1.036	0.952
R_o, equilibrium I−Br distance, Å	3.012	3.053
ground-state harmonic frequency, cm^{-1}	136.8	127.4
Morse Fit Parameters		
D(Morse), eV	1.023	0.950
R_o(Morse), Å	3.012	3.057
a (Morse exponent), $Å^{-1}$	1.334	1.222

In this section, we consider analytically and by means of computer simulations an effect that may play a larger role in IBr_2^- and $BrICl^-$, compared to I_3^-, namely, the effect of the proximity to the dissociation threshold on wave packet dynamics in highly excited vibrational states. We show that the revivals of the IBr^- wave packet may be smeared by a high-order anharmonicity near the threshold. While the following theoretical analysis is not a unique interpretation of the experiment, we believe that it is of general interest.

The time-dependent wave function of a packet is given by

$$\psi(x,t) = \sum_v c_v u_v(x) \exp[-iE(v)t/\hbar] \quad (2)$$

where v is the vibrational quantum number, and c_v and $u_v(x)$ are the level amplitudes and spatial wave functions. The initial wave packet created in the experiment is real and localized; for a short time, it behaves classically.[34−36] The pump−probe experiment measures the wave packet position with a finite resolution, and during this short time, we observe oscillations in the signal.

The delocalization of the wave packet and its subsequent revivals come about because the levels $E(v)$ of a quantum system are not uniformly spaced.[32,33] The anharmonicity can be accounted for by expanding the level energies in a Taylor series as a function of v:

$$E(v) = E(\bar{v}) + (v - \bar{v})\left.\frac{\partial E}{\partial v}\right|_{\bar{v}} + \frac{(v - \bar{v})^2}{2!}\left.\frac{\partial^2 E}{\partial v^2}\right|_{\bar{v}} + \frac{(v - \bar{v})^3}{3!}\left.\frac{\partial^3 E}{\partial v^3}\right|_{\bar{v}} + \ldots \quad (3)$$

where $\bar{v}$ is the average level quantum number of the wave packet. Equation 3 can be rewritten in the form[32,33]

$$E(v) = E(\bar{v}) + 2\pi h\frac{(v - \bar{v})}{T_{cl}} \pm 2\pi h\frac{(v - \bar{v})^2}{T_{rev}} \pm 2\pi h\frac{(v - \bar{v})^3}{T_d} + \ldots \quad (4)$$

where $\pm$'s denote the signs of the respective derivatives in eq 3, $T_{cl} = 2\pi/\omega$ is the classical vibrational period,

$$T_{rev} = 2T_{cl}\left|\hbar\frac{\partial\omega}{\partial E}\right|^{-1} \quad (5)$$

is the wave packet "revival" period,[32,33] and

$$T_d = 6T_{cl}\left|\hbar^2\frac{\partial}{\partial E}\left(\omega\frac{\partial\omega}{\partial E}\right)\right|^{-1} \quad (6)$$

is a new time scale whose meaning is explained below. Higher order time scales involved in the expansion in eq 4 can be defined in a similar way.

In the well-known case corresponding to the Morse oscillator, expansion (3−4) is cut off after the quadratic term, which describes the first-order anharmonicity. If all higher order terms are neglected or identically zero (as for the Morse oscillator), the wave packet dynamics involve two time scales: the classical period T_{cl} (given by the linear term) and the revival period T_{rev} {quadratic term).[32,33] However, neglecting the cubic and other higher order terms is justified only if the anharmonicity is described by a single parameter. In real systems, this is usually not the case and, in addition to the classical period and revival time, other time scales starting with T_d (eq 6) are involved in the dynamics. Similar to the cessation of classical oscillations, the periodic revivals of the wave packet should cease after a certain propagation time, as the cubic and higher order terms in eq 4, substituted into time-dependent eq 2, become nonnegligible. The smearing of the revival structure is described by the cubic term in eq 4. If the quadrupole and higher order terms can be neglected, T_d represents the period of subsequent reconstructions of the revival structure (i.e., second-order revivals).

For the Morse oscillator, the frequency scaling with energy is given by eq 1, and T_d, as given by eq 6, is identically 1/0 or infinity, independent of energy. Therefore, on a Morse potential, the wave packet dynamics are strictly described in terms of oscillations and periodic revivals. Below, we show that for a general potential the higher-order terms "explode" near the dissociation threshold.

For the revival picture to be valid, the condition for neglecting the cubic and higher-order terms in eq 4 must be satisfied:

$$1/T_{rev} \gg |v - \bar{v}|/T_d \quad (7)$$

Using a general power law for the long-range scaling of the potential,

$$V(R) = -aR^{-n} \quad (8)$$

it is easy to show that the frequency threshold law is

$$\omega(E) = \alpha E^{(1/2+1/n)} \quad (9)$$

where a and α are constants. Using eqs 5, 6, and 9, eq 7 leads to

$$E \gg \left(\frac{2h\alpha}{3n}\left|v - \bar{v}\right|\right)^{\frac{2n}{n-2}} \quad (10)$$

Near the dissociation threshold, $E \rightarrow 0$, the condition of eq 10 breaks down and with it the periodic revival picture of the wave packet dynamics. Because this condition must be valid for all terms with significant amplitude in eq 2, we must consider the case of $|v - \bar{v}| \approx N$, where N is the number of vibrational levels in the wave packet. For potentials with $n > 2$, the number of bound levels is finite, and N scales as $N \propto \Delta E/\omega \propto |dV/dR|/\omega$, where the potential gradient is taken at the initial wave packet position. In our experiments, the initial position is on the inner wall of the IBr^- potential and both the energy range ΔE and the level density (proportional to $1/\omega$) increase with E_v. Therefore, N is increasing rapidly near the dissociation threshold. In the simplest approximation, the energy spread is given by the reflection principle, projecting the parent (IBr_2^-) ground-state wave function on the quantum levels of the fragment (IBr^-). Ballpark estimates give $\Delta E \approx 0.5$ V.

For near-threshold IBr^-, the long-range potential is best characterized by the ion−neutral interaction, which scales as R^{-4} (i.e., $n = 4$). For this type of potential, the number of bound levels in the energy region between $E_v = 0.8D_o$ and the dissociation threshold is $N \approx 10^2$. Estimating other relevant parameters, the right-hand side of eq 10 is ~0.08 eV, meaning that the revival picture of the wave packet dynamics is valid only for $E_v \ll 0.92D_o$.

To check the above analysis, we performed time-dependent wave packet propagations on the MP2 and QCISD potentials shown in Figure 8. The wave function was represented on an equally spaced grid of 2048 points ranging from 1.7 to 15 Å. We used the Fourier method to perform the kinetic energy operation.[59,60] To construct the potential from the ab initio calculated points, spline interpolation was used. The initial wave function was represented by a Gaussian function with full width of 0.1 Å, located at the inner turning point of the potential with a varying average energy (E_v). The propagation in time was carried out by a Chebychev polynomial expansion of the evolution operator.[61,62] An optical potential was added to the far end of the grid to absorb all continuous parts of the wave packet.[63] The expected experimental signal is calculated by a convolution of the square of the wave function with a Gaussian window function, located at $R = 4.5$ and 0.4 Å wide, representing the probe pulse absorption.[23] This method assumes a weak and impulsive probe step.

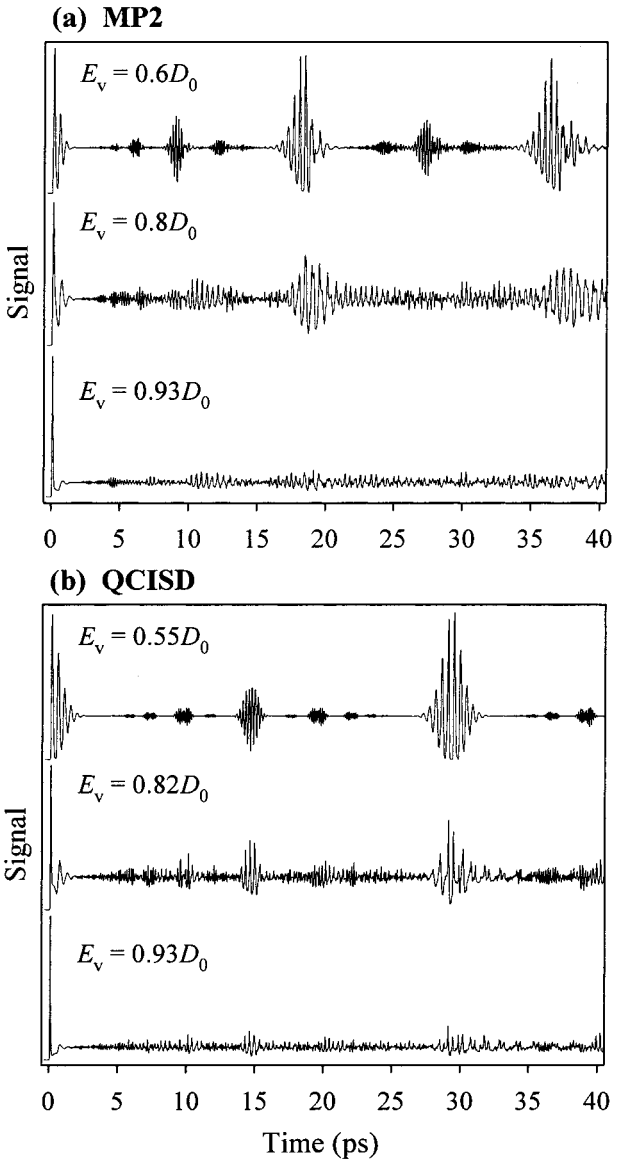

Figure 9. IBr^- absorption signals calculated by propagating vibrational wave packets on the (a) MP2 and (b) QCISD potentials, shown in parts a and b of Figure 8, respectively, assuming different degrees of vibrational excitation (as indicated in the figure). See the text for details. The signals are normalized relative to the initial peak intensity.

Parts a and b of Figure 9 show the calculated signals for the MP2 and QCISD potentials, respectively, assuming different degrees of vibrational excitation. All signals are normalized relative to the initial peak intensity. At moderate excitations ($E_v < 0.6D_o$), the signal follows the expected revival structure,[32,33] and complete and partial revivals of various orders are clearly observed. At higher energies ($E_v \approx 0.8D_o$) the revivals of the wave packet become less intense, and closer to the threshold ($E_v > 0.9D_o$) they are lost entirely. As stated in section V.B., the MP2 and QCISD potentials deviate in the long range from the expected R^{-4} scaling law. To correct for the long-range ab initio errors, we constructed a potential consisting of the ab initio QCISD points up to $R = 8$ Å ($E = 0.026$ eV). From this point on, the potential was extrapolated using an R^{-4} function. The wave packet propagation results obtained using this potential are similar to Figure 9b.

The IBr^- vibrational excitation ($E_v \approx 0.9D_o$) observed in IBr_2^- photodissociation corresponds to the near-threshold regime where higher order time scales are important. On the other hand, in the Neumark experiment on gas-phase I_3^-,[12,13] the vibrational excitation of I_2^- of $\sim 0.7D_o$ corresponds to the intermediate regime where the smearing of the early wave packet revivals only begins to be important.

Other important observations based on Figure 9 include: the initial oscillations cease faster closer to D_o, because of the increase in N; the predicted revival times (for $E_v < 0.9D_o$) are very sensitive to details of the potential. For the MP2 potential, the complete revivals of the orders of $^1/_2$ and 1 are observed at 18 and 36 ps, respectively, while for the QCISD potential the order $^1/_2$ revival occurs at 29 ps. (An order $^1/_2$ revival is a complete revival with a phase shift of π.)[32,33] Thus, the predicted revival periods are $T_{rev}(MP2) = 36$ ps and $T_{rev}(QCISD) = 58$ ps. This compares to the experimental observation by Zanni et al. of the order $^1/_2$ and 1 revivals in I_2^- at 45 and 90.5 ps, respectively,[12,13] corresponding to $T_{rev}(I_2^-) = 90.5$ ps.

VI. Summary

This work is the first study of mixed trihalide anions in the gas phase. We reported the photochemistry and photodissociation dynamics of $BrICl^-$ and IBr_2^- anions near 400 nm. For $BrICl^-$, we observe two major photodissociation channels, yielding IBr^- and ICl^- with a branching ratio of $\sim$4:1, which varies slightly depending on the wavelength. The photodissociation of IBr_2^- yields primarily IBr^- anion products. No $BrCl^-$ and Br_2^- products are formed from $BrICl^-$ and IBr_2^-, respectively, and the parent anions are ascribed linear $[Br-I-Cl]^-$ and $[Br-I-Br]^-$ structures, in agreement with ab initio calculations. Small (<5%) yields of atomic anion fragments are also observed. The IBr^- and ICl^- fragments are formed in highly excited vibrational states, and their dynamics are probed by femtosecond pump−probe fragment mass spectroscopy. We observe vibrational coherence in IBr^- products corresponding to excitations of $\sim 0.8D_o(IBr^-)$ in $BrICl^-$ dissociation, and up to $\sim 0.9D_o$ in IBr_2^- dissociation. The high degrees of vibrational excitation raise questions about the effect of the proximity to the dissociation threshold on the dynamics of coherent wave packets. We have analyzed these dynamics both analytically and by means of wave packet simulations and shown that additional, higher order time scales begin to play a role, in addition to the periods of classical vibrations and wave packet revivals. The higher order time scales are due to the nonlinear anharmonicity of the potential and become important near the threshold, resulting in the smearing of wave packet revivals.

Acknowledgment. The authors would like to thank Jan M. L. Martin for advice on the DFT calculations, Erez Gershgoren and Sandy Ruhman for communicating unpublished experimental results, Martin T. Zanni for a preprint of the paper,[13] and Robert Parson for helpful discussions. L.J.B. and R.K. thank JILA (a joint institute of the University of Colorado and the National Institute for Standards and Technology) for the Visiting Fellowships. This work is supported by the National Science Foundation.

References and Notes

(1) Banin, U.; Waldman, A.; Ruhman, S. *J. Chem. Phys.* **1992**, *96*, 2416.
(2) Banin, U.; Kosloff, R.; Ruhman, S. *Isr. J. Chem.* **1993**, *33*, 141.
(3) Banin, U.; Ruhman, S. *J. Chem. Phys.* **1993**, *99*, 9318.
(4) Banin, U.; Ruhman, S. *J. Chem. Phys.* **1993**, *98*, 4391.
(5) Banin, U.; Bartana, A.; Ruhman, S.; Kosloff, R. *J. Chem. Phys.* **1994**, *101*, 8461.
(6) Banin, U.; Kosloff, R.; Ruhman, S. *Chem. Phys.* **1994**, *183*, 289.
(7) Gershgoren, E.; Gordon, E.; Ruhman, S. *J. Chem. Phys.* **1997**, *106*, 4806.

(8) Gershgoren, E.; Banin, U.; Ruhman, S. *J. Phys. Chem. A* **1998**, *102*, 9.
(9) Kühne, T.; Vöhringer, P. *J. Chem. Phys.* **1996**, *105*, 10788.
(10) Kühne, T.; Kuster, R.; Vöhringer, P. *Chem. Phys.* **1998**, *233*, 161.
(11) Kühne, T.; Vöhringer, P. *J. Phys. Chem. A* **1998**, *102*, 4177.
(12) Zanni, M. T.; Greenblatt, B. J.; Davis, A. V.; Neumark, D. M. *Proc. SPIE* **1998**, *3271*, 196.
(13) Zanni, M. T.; Greenblatt, B. J.; Davis, A. V.; Neumark, D. M. *J. Chem. Phys.*, in press.
(14) Johnson, A. E.; Myers, A. B. *J. Phys. Chem.* **1996**, *100*, 7778.
(15) Dantus, M.; Bowman, R. M.; Baskin, J. S.; Zewail, A. H. *Chem. Phys. Lett.* **1989**, *159*, 406.
(16) Dantus, M.; Bowman, R. M.; Gruebele, M.; Zewail, A. H. *J. Chem. Phys.* **1989**, *91*, 7437.
(17) Bowman, R. M.; Dantus, M.; Zewail, A. H. *Chem. Phys. Lett.* **1989**, *156*, 131.
(18) Pedersen, S.; Baumert, T.; Zewail, A. H. *J. Phys. Chem.* **1993**, *97*, 12460.
(19) Pugliano, N.; Palit, D. K.; Szarka, A. Z.; Hochstrasser, R. M. *J. Chem. Phys.* **1993**, *99*, 7273.
(20) Pugliano, N.; Szarka, A. Z.; Gnanakaran, S.; Triechel, M.; Hochstrasser, R. M. *J. Chem. Phys.* **1995**, *103*, 6498.
(21) Pugliano, N.; Szarka, A. Z.; Hochstrasser, R. M. *J. Chem. Phys.* **1996**, *104*, 5062.
(22) Gnanakaran, S.; Lim, M.; Pugliano, N.; Volk, M.; Hochstrasser, R. M. *J. Phys. Condens. Mater.* **1996**, *8*, 9201.
(23) Ashkenazi, G.; Banin, U.; Bartana, A.; Kosloff, R.; Ruhman, S. *Adv. Chem. Phys.* **1997**, *100*, 229.
(24) Bartana, A.; Banin, U.; Ruhman, S.; Kosloff, R. *Chem. Phys. Lett.* **1994**, *229*, 211.
(25) Benjamin, I.; Banin, U.; Ruhman, S. *J. Chem. Phys.* **1993**, *98*, 8337.
(26) Benjamin, I. *J. Chem. Phys.* **1995**, *103*, 2459.
(27) Benjamin, I.; Barbara, P. F.; Gertner, B. J.; Hynes, J. T. *J. Phys. Chem.* **1995**, *99*, 7557.
(28) Lynden-Bell, R. M.; Kosloff, R.; Ruhman, S.; Danovich, D.; Vala, J. *J. Chem. Phys.* **1998**, *109*, 9928.
(29) Sato, H.; Hirata, F.; Myers, A. B. *J. Phys. Chem. A* **1998**, *102*, 2065.
(30) Choi, H.; Bise, R. T.; Hoops, A. A.; Neumark, D. M., 1999. In preparation.
(31) Gershgoren, E.; Ruhman, S. Private communication.
(32) Averbukh, I. S.; Perelman, N. F. *Sov. Phys. Usp.* **1991**, *34*, 572.
(33) Averbukh, I. S.; Perelman, N. F. *Phys. Lett. A* **1989**, *139*, 449.
(34) Bohr, N. *Z. Phys.* **1923**, *13*, 117.
(35) Schrödinger, E. *Naturwiss.* **1926**, *14*, 664.
(36) Landau, L. D.; Lifshitz, E. M. *Quantum Mechanics: Nonrelativistic Theory*, 3rd ed.; Pergamon Press: Oxford, 1977.
(37) Frisch, M. J.; Trucks, G. W.; Schlegel, H. B.; Scuseria, G. E.; Robb, M. A.; Cheeseman, J. R.; Zakrzewski, V. G.; Montgomery, J. A.; Stratmann, R. E.; Burant, J. C.; Dapprich, S.; Millam, J. M.; Daniels, A. D.; Kudin, K. N.; Strain, M. C.; Farkas, O.; Tomasi, J.; Barone, V.; Cossi, M.; Cammi, R.; Mennucci, B.; Pomelli, C.; Adamo, C.; Clifford, S.; Ochterski, J.; Petersson, G. A.; Ayala, P. Y.; Cui, Q.; Morokuma, K.; Malick, D. K.; Rabuck, A. D.; Raghavachari, K.; Foresman, J. B.; Cioslowski, J.; Ortiz, J. V.; Stefanov, B. B.; Liu, G.; Liashenko, A.; Piskorz, P.; Komaromi, I.; Gomperts, R.; Martin, R. L.; Fox, D. J.; Keith, T.; Al-Laham, M. A.; Peng, C. Y.; Nanayakkara, A.; Gonzalez, C.; Challacombe, M.; Gill, P. M. W.; Johnson, B. G.; Chen, W.; Wong, M. W.; Andres, J. L.; Head-Gordon, M.; Replogle, E. S.; Pople, J. A. *Gaussian 98*; revision A.1; Gaussian, Inc.: Pittsburgh, PA, 1998.
(38) Adamo, C.; Barone, V. *J. Chem. Phys.* **1998**, *108*, 664.
(39) Wadt, W. R.; Hay, P. J. *J. Chem. Phys.* **1985**, *82*, 284.
(40) Glukhovtsev, M. N.; Pross, A.; Radom, L. *J. Am. Chem. Soc.* **1995**, *117*, 2024.
(41) Greenblatt, B. J.; Zanni, M. T.; Neumark, D. M. *Chem. Phys. Lett.* **1996**, *258*, 523.
(42) Zanni, M. T.; Taylor, T. R.; Greenblatt, B. J.; Soep, B.; Neumark, D. M. *J. Chem. Phys.* **1997**, *107*, 7613.
(43) Do, K.; Klein, T. P.; Pommerening, C. A.; Sunderlin, L. S. *J. Am. Soc. Mass Spectrom.* **1997**, *8*, 688.
(44) Nadal, M. E.; Kleiber, P. D.; Lineberger, W. C. *J. Chem. Phys.* **1996**, *105*, 504.
(45) Johnson, M. A.; Lineberger, W. C. Pulsed Methods for Cluster Ion Spectroscopy. In *Techniques for the Study of Ion Molecule Reactions*; Farrar, J. M., Saunders, J. W., Eds.; Wiley: New York, 1988; p 591.
(46) Klar, D.; Ruf, M. W.; Hotop, H. *Aust. J. Phys.* **1992**, *45*, 263.
(47) Klar, D.; Ruf, M. W.; Hotop, H. *Chem. Phys. Lett.* **1992**, *189*, 448.
(48) Ziesel, J. P.; Nenner, I.; Schulz, G. J. *J. Chem. Phys.* **1975**, *63*, 1943.
(49) Ziesel, J. P.; Schulz, G. J.; Milhaud, J. *J. Chem. Phys.* **1975**, *62*, 1936.
(50) Mamyrin, B. A.; Karataev, V. I.; Shmikk, D. V.; Zagulin, V. A. *Sov. Phys. JEPT* **1973**, *37*, 45.
(51) Alexander, M. L. Ph.D. Thesis, University of Colorado, 1987.
(52) Vorsa, V.; Campagnola, P. J.; Nandi, S.; Larsson, M.; Lineberger, W. C. *J. Chem. Phys.* **1996**, *105*, 2298.
(53) Nadal, M. E. Ph.D. Thesis, University of Colorado, 1996.
(54) Averbukh, I. S.; Vrakking, M. J. J.; Villeneuve, D. M.; Stolow, A. *Phys. Rev. Lett.* **1996**, *77*, 3518.
(55) Møller, C.; Plesset, M. S. *Phys. Rev.* **1934**, *46*, 618.
(56) Pople, J. A.; Seeger, R.; Krishnan, R. *Int. J. Quantum Chem. Symp.* **1977**, *11*, 149.
(57) Bartlett, R. J. Many Body Perturbation Theory and Coupled Cluster Theory for Electron Correlation in Molecules. In *Annu. Rev. Phys. Chem.*; Rabinovitch, B. S., Schurr, J. M., Strauss, H. L., Eds.; Annual Reviews, Inc.: Palo Alto, CA, 1981; Vol. 32; p 359.
(58) Pople, J. A.; Headgordon, M.; Raghavachari, K. *J. Chem. Phys.* **1987**, *87*, 5968.
(59) Kosloff, D.; Kosloff, R. *J. Comput. Phys.* **1983**, *52*, 35.
(60) Kosloff, R. Quantum Molecular Dynamics on Grids. In *Dynamics of Molecules and Chemical Reactions*; Wyatt, R. E., Zhang, J. Z., Eds.; Marcel Dekker: New York, 1996; p 185.
(61) Tal Ezer, H.; Kosloff, R. *J. Chem. Phys.* **1984**, *81*, 3967.
(62) Kosloff, R. *Annu. Rev. Phys. Chem.* **1994**, *45*, 145.
(63) Kosloff, R.; Kosloff, D. *J. Comput. Phys.* **1986**, *63*, 363.
(64) Kaya, K.; Mikami, N.; Udagawa, Y.; Ito, M. *Chem. Phys. Lett.* **1972**, *16*, 151.